Experimental and Modeled Output Characteristics of a Compact, Passively Q-Switched Tm:YLF Laser

Stephen R. Chinn, *Life Senior Member, IEEE*, Lew Goldberg, Vernon King, Jeffrey H. Leach, Alan D. Hays, and Brian Cole

***Abstract*— We measure the output characteristics of a compact, laser diode end-pumped Tm:YLF laser, operated in continuous wave (CW) mode, or passively Q-switched (PQS) using various Cr^{2+}:ZnS saturable absorbers. A numerical Finite-Difference Beam Propagation Method (FD-BPM) is developed and used to model the laser CW and pulsed performance. Good agreement between the experiment and simulated output is demonstrated. The 39 mm-long laser resonator utilizes a 20.2 mm-long Tm:YLF crystal, a 1908 nm volume Bragg grating (VBG) reflector to restrict the emission wavelength, and an intra-cavity negative lens to reduce the energy fluence in the saturable absorber. A laser utilizing a Cr^{2+}:ZnS saturable absorber with 91.9% unsaturated transmission generates 9.8 mJ PQS pulses with 8.7 ns full-width-half-maximum (FWHM) pulse duration. Maximum average output powers of 6.1 W and 6.5 W are generated in PQS and CW operation, respectively.**

***Index Terms*— Solid state lasers, 2 μm laser, thulium, Tm:YLF, Q-switching, passive Q-switch, saturable absorber, Cr:ZnS, VBG, BPM, FD-BPM.**

I. Introduction

PULSED lasers operating in the eye-safe 2 μm spectral band are needed for several applications, such as laser range-finding (LRF), light detection and ranging (LIDAR), long-range gated imaging, medical uses [1], pumping of optical parametric oscillators (OPOs) for generating long-wave and mid-infrared [2] radiation, and non-linear harmonic generation of near-IR, visible, and UV radiation [3]. In addition to large pulse energy, these applications also benefit from a short pulse duration and high peak power. A narrow emission spectrum is also beneficial since it allows improved suppression of broad-band background emission using narrow band-pass filters. Although Tm-doped fiber sources can generate very high average powers, a bulk gain medium solid state laser can generate higher pulse energies and peak powers in a much smaller device. For nonlinear conversion processes, higher peak powers are particularly important since they allow the use of larger pump beam diameters, reducing impact of beam diffraction and beam walk-off in the nonlinear crystal, and decreasing the magnitude of thermal lensing. For LRF and LIDAR, a larger pulse energy increases the maximum operating range, and a shorter pulse duration improves the range resolution. Due to the efficiency advantage offered by the cross relaxation process which yields two excited-state ions for each pump photon [4], Tm-doped crystal hosts [2], [3], [4], [5], [6], [7], [8], [9], [10], [11], [12], [13], [14], [15], [16] are the favored solid-state laser gain materials for generation of emission near 2 μm. Compared to other Tm-doped crystals, Tm:YLF offers the significant advantage of a very low thermo-optic coefficient, reducing the effect of thermal lensing that can cause significant changes in the laser output characteristics with pump power.

Both active and passive Q-switching (PQS) Tm:YLF and Tm:YAP lasers have been explored [8], [9], [10], [11], [12], [13], [14], [15], [16]. A maximum pulse energy of 10.5 mJ, with 22 ns pulse duration, was generated using an acousto-optic-modulator (AOM) Q-switched Tm:YLF laser operating at a pulse repetition frequency (PRF) of 10 Hz [8]. A simpler Q-switching technique based on a vibrating mirror has been also been successfully used with Tm:YAP lasers [9]. Compared to the AOM-active Q-switching, PQS offers significant reductions in laser complexity, size and cost. In addition, since no radio frequency (RF) driver is needed, PQS lasers can achieve higher overall laser electrical efficiency than AOM Q-switched versions. Recently, Tm:YLF and Tm:YAP PQS lasers using Cr^{2+}:ZnS and Cr^{2+}:ZnSe saturable absorbers have been reported [10], [11], [12], [13], [14], [15], [16]. A passively-Q-switched laser (PQSL) with Tm:YLF and a Cr^{2+}:ZnSe saturable absorber generated 4.2 mJ, 26 ns-long pulses, corresponding to a peak power of 162 kW peak power [14]. A two-channel spectrally combined Tm:YLF laser with Bragg gratings (VBGs) and a Cr^{2+}:ZnS saturable absorber, generated 5.8 mJ, 90 ns pulses [15]. A 230 mm-long Tm:YLF PQSL utilizing Cr^{2+}:ZnS with an unsaturated PQS transmission (T_Q) of 89% generated 10 mJ, 29 ns-long pulses at 1886 nm, corresponding to a peak power of 350 kW [2]. Highest peak powers of 520-600 kW were achieved in Tm:YLF PQSLs with 45 mm, 100 mm, 130 mm-long cavities, generating pulse energies and pulse durations of 3.7 mJ, 10.8 mJ, 15.6 mJ and 7.1 ns, 19.7 ns, 26 ns, respectively [16].

In this paper, we describe a 39 mm-long Tm:YLF PQSL that incorporates an intra-cavity negative lens to prevent optical damage in Cr^{2+}:ZnS by expanding the laser mode and reducing the energy fluence in the saturable absorber. The laser generates a maximum pulse energy of 9.8 mJ, with a pulse duration of 8.7 ns, corresponding to a maximum peak pulse power of 1.1 MW. In addition, we implement a

Manuscript received 7 November 2022; revised 8 March 2023; accepted 12 March 2023. Date of publication 22 March 2023; date of current version 5 April 2023. This work was supported by the U.S. Army DEVCOM C5ISR Research and Technology Integration (RTI) Directorate. *(Corresponding author: Lew Goldberg.)*

Stephen R. Chinn is with Fibertek Inc., Herndon, VA 20107 USA (e-mail: stephen.r.chinn.ctr@army.mil).

Lew Goldberg, Vernon King, Jeffrey H. Leach, Alan D. Hays, and Brian Cole are with the U.S. Army Combat Capabilities Development Command, Research and Technology Integration Directorate, Fort Belvoir, VA 22060 USA (e-mail: lew.goldberg.civ@army.mil; vernon.king.civ@army.mil; jeffrey.h.leach.civ@army.mil; alan.d.hays.civ@army.mil; brian.j.cole1.civ@army.mil).

Digital Object Identifier 10.1109/JQE.2023.3260190

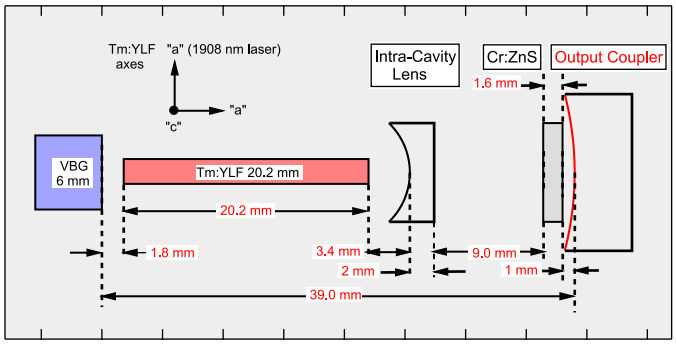

Fig. 1. PQSL schematic cavity configuration and Tm:YLF crystal orientation.

numerical Finite-Difference, Beam Propagation Method (FD-BPM) whose inputs come from measured or published parameters. This model demonstrates good agreement between the measured and simulated laser output characteristics.

II. Experimental Configuration

Fig. 1 shows the Tm:YLF PQSL cavity, formed by a high-reflectance VBG (IPG OptiGrate) mirror on one end and a partially reflecting concave output coupler (OC) mirror on the other. An f = −12.5mm plano-concave negative lens, placed close to the Tm:YLF crystal, expands the laser mode in the Cr^{2+}:ZnS (IPG Photonics) saturable absorber, positioned near the output coupler. This is found to be required in order to keep the intra-cavity energy fluence in the AR-coated Cr^{2+}:ZnS below its optical damage level, measured to be in the range of 3-4 J/cm^2 for 1908 nm, 20 ns-long pulses. To further reduce the intra-cavity energy fluence, an output coupler (25 mm radius of curvature) with a relatively low reflectivity of R=36% is selected. The refractive indices we use are Tm:YLF=1.44, fused silica lens=1.44, and Cr:ZnS=2.23. We measure the top-hat-equivalent mode area, at the concave side of the output coupler, to be approximately 1.8 mm^2 at the maximum laser pump power. The laser operates in fundamental mode under CW and PQS conditions, with a 74 mrad output beam divergence, and a beam quality factor of M^2 = 1.2. Three versions of PQSL were implemented, each incorporating Cr^{2+}:ZnS elements with directly measured 1908 nm unsaturated transmissions T_Q = 91.9%, 92.3%, 93.3%, with corresponding thicknesses of 1.6 mm, 1.6 mm, and 1.4 mm. The Tm:YLF crystal (AC Materials) has a 3.5 atomic-% Tm concentration, and measures 20.2 × 4.0.×1.5 mm along the crystallographic a, c, a, crystal axes, respectively. The 4.0 ×1.5 mm faces of the crystal are anti-reflection (AR) coated for the pump and laser wavelengths. For heat dissipation, the crystal is mounted in a water-cooled copper heat-sink with an indium foil thermal interface, and a 22°C heat-sink temperature is maintained. All laser components, with the exception of the pump diode, are mounted on a small aluminum plate.

As described previously [16], the laser is end pumped through the 6.0 mm-thick, AR-coated VBG by a fiber-coupled (105 μm core diameter, numerical aperture of 0.22) laser diode (n-Light) that is temperature-controlled to emit at 792 nm. Pump transmission through the VBG (AR coated at 792 nm and 1908 nm) is measured to be 93%, and its reflectivity is >99% over a 0.3 nm-wide spectral band centered at 1907.8 nm. A single f = 18mm aspheric lens collects the pump light from the fiber, and relays a magnified image of the fiber core top-hat intensity distribution inside the Tm:YLF crystal. The pump image magnification factor is determined by fiber-to-lens and lens-to-crystal distances. Longitudinal position of the image was optimized by adjusting the fiber-to-lens distance until maximum output power was achieved. For the maximum pump power of 27.2W incident on the Tm:YLF (28.9 W incident on the VBG), we measure a pump absorption fraction of 93% under non-lasing conditions, and 97% under lasing conditions. The un-attenuated pump intensity distribution in the Tm:YLF is calculated from the results of an optics ray-trace program. Ray densities at 0.1 mm separations are post-processed to yield the radially symmetric, un-attenuated intensity distribution, which is then used as an initial state in the numerical model, described below. Fig. 2(a) shows a false-color image of this (r,z)-dependent pump intensity distribution, normalized for 1W incident pump power. This example has a fiber-core magnification factor of 5.33, resulting in a top hat pump spot diameter of 560 μm, positioned inside the crystal at a distance of z = 8 mm from the pumped end of the crystal. Other simulations show that 1-2 mm changes in the spot z-position do not have a significant impact on laser performance. In this example, the minimum pump spot FWHM diameter of 510 μm occurs at the input face of the Tm:YLF. Significant changes in the pump distribution occur due to pump absorption, pump saturation, and lasing intensity. The resulting pump distribution is calculated by our numerical model described below, and is shown in Fig. 2(b) for CW laser operation and pump power of 28.9 W.

III. Experimental Results

A. CW Operation

To determine the base-line performance of the laser, its output characteristics are first measured under CW operation. For power measurements, a long-pass spectral filter is used to block residual pump power before the laser output impinges on the power head (Ophir L30A-SH). In order to allow a meaningful comparison between laser CW and Q-switched output average output powers, for the CW measurements, a 3 mm-thick AR coated fused silica plate is inserted into the cavity at a position close to the output coupler. This plate serves as a surrogate to make the laser resonator mode diameter nearly the same as it is with the 1.6 mm-thick, T_Q = 91.9% and 92.3% saturable absorbers in the cavity. CW output powers, measured as a function of pump powers incident on the VBG are shown in Fig. 3. Predictions of the numerical model, to be discussed below, are also plotted. We measure a 6.55 W maximum output power, 14 W lasing threshold, and 0.439 optical slope efficiency. After correcting for the 7% pump loss in the VBG, the slope efficiency, referenced to the pump power incident on the VBG, is 0.472. Significantly higher CW output powers and slope efficiencies could be achieved with output mirror reflectivities larger than the 36% value required to reduce the intra-cavity energy fluence.

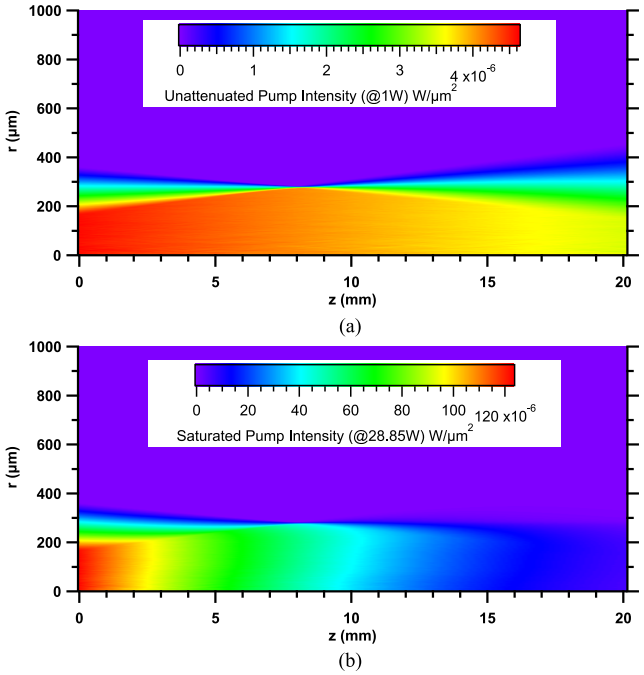

Fig. 2. (a) Calculated un-attenuated pump intensity distribution in the 20.2 mm long Tm:YLF crystal, shown vs. propagation distance, z (horizontal axis) from pumped face of crystal and radial dimension, r (vertical axis). (b) Calculated pump distribution with effects of absorption, pump saturation, and laser saturation during CW lasing in the 20.2-mm-long Tm:YLF crystal, shown vs. propagation distance, z (horizontal axis) from pumped face of crystal and radial dimension, r (vertical axis).

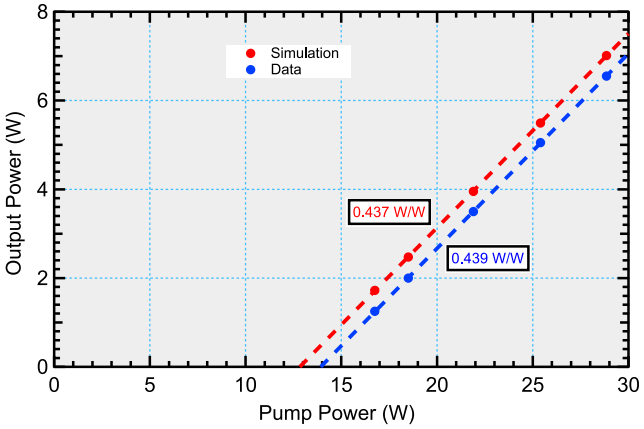

Fig. 3. Measured and simulated output power of the laser operating under CW conditions vs. pump power incident on the VBG.

Laser emission spectra, measured using a fiber-coupled spectrum analyzer (Yokogawa AQ6375) with 0.05 nm resolution, are shown in Fig. 4 for CW and PQSL operation, with the VBG reflectivity spectrum also displayed. The reflectivity spectrum is calculated from the VBG transmission spectrum measured using a broad-band super-luminescent laser source.

The VBG reflectivity band has a linewidth of 0.6 nm FWHM, and 0.47 nm when measured between 90% reflectivity points.

The CW laser emission spectrum, centered near the 1907.8 nm center of the VBG reflectivity band, has a linewidth of 0.3 nm FWHM, and 0.48 nm when measured between 10% intensity points. A similar linewidth is measured for the PQSL, with its spectrum slightly blue-shifted. Both measurements are

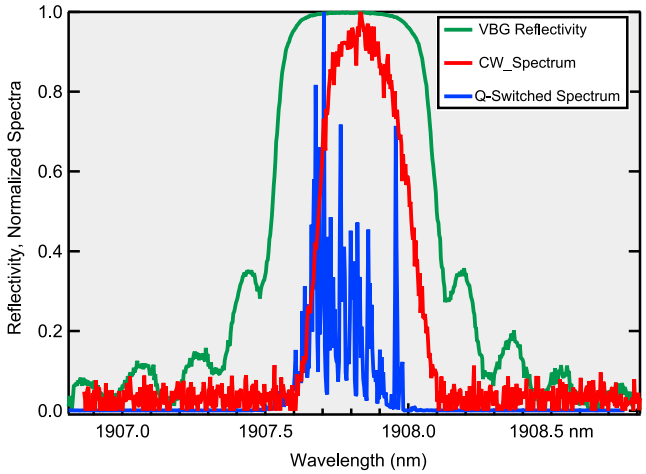

Fig. 4. Laser emission spectra for CW and Q-switched operation with overlaid reflectivity spectrum of the VBG.

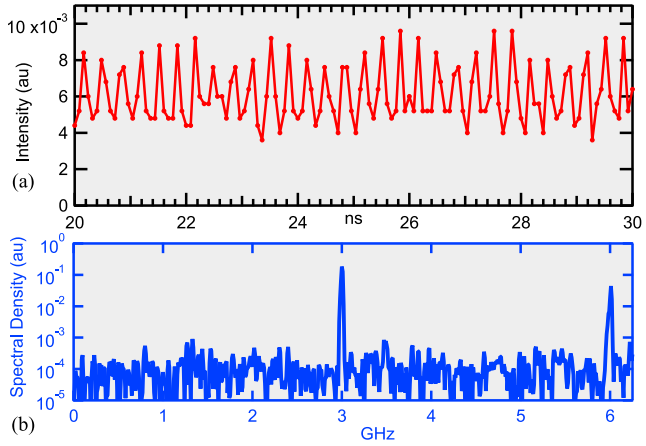

Fig. 5. (a) Temporal trace of CW laser power variations, and (b) its Fourier transform.

carried out at a pump power of 22 W, with the PQSL utilizing Cr^{2+}:ZnS with $T_Q = 92.3\%$.

Temporal variations in the CW laser power (at a pump power of 22 W) are measured by a 10 GHz-bandwidth detector (EOT ET-5000) and a 12.5 GHz-bandwidth oscilloscope (Tektronix 71254C). The observed variations are dominated by near-sinusoidal modulation with a period of approximately 0.3 ns, as shown by a 10 ns-long section of the oscilloscope data displayed in Fig. 5(a), where power fluctuations are approximately +/-20% about the mean value. A Fourier transform of the temporal trace, Fig. 5(b), clearly shows the primary frequency component at 3 GHz, and a second harmonic at 6 GHz. We attribute this intensity modulation to beating between the longitudinal modes of the laser. After accounting for all elements inside the laser resonator, its effective optical path length is 50.0 mm, so that the laser longitudinal mode spacing is calculated to be 3.00 GHz, in excellent agreement with the measured modulation frequency.

B. Q-Switched Operation

Measured average output powers of Q-switched lasers with $T_Q = 91.9\%$, 92.3% and 93.3% are shown in Figs. 6(a), 6(b) and 6(c), respectively. Maximum average powers of 6.1W, 6.25 W and 6.8 W are measured for the three laser variants,

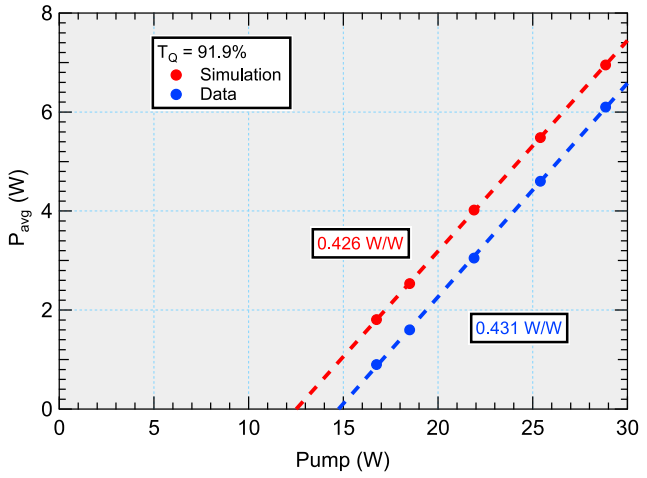

(a)

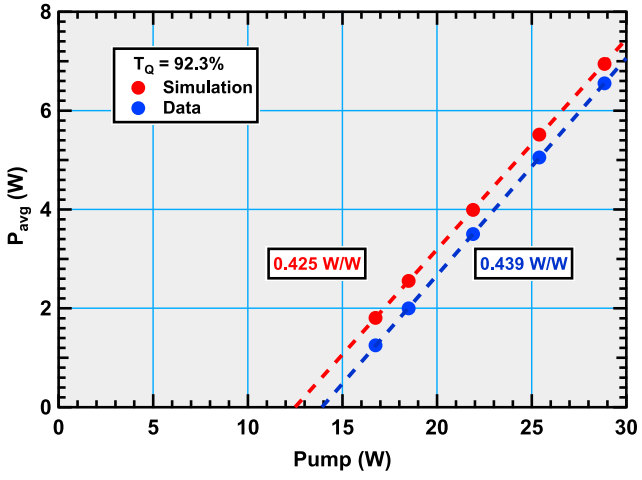

(b)

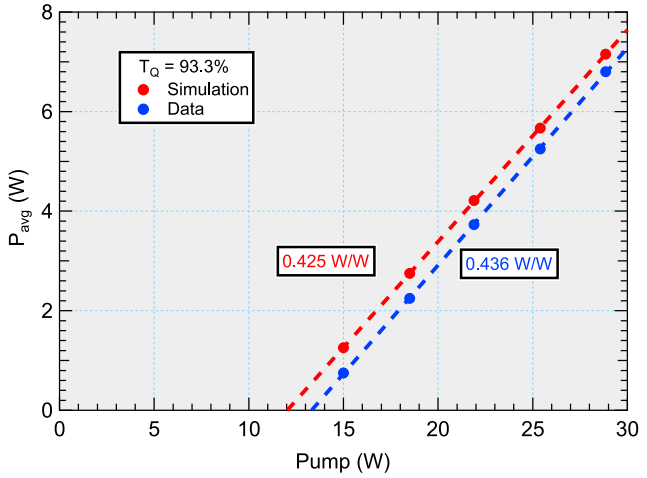

(c)

Fig. 6. (a). Average laser power vs. pump power for T_Q = 91.9% (b). Average laser power vs. pump power for T_Q = 92.3% (c). Average laser power vs. pump power for T_Q = 93.3%.

respectively. The slope efficiencies of 0.43, 0.43, and 0.44 are nearly the same as for the CW laser. The average power of the laser with the T_Q = 93.3%, 1.4 mm thick Cr^{2+}:ZnS is slightly higher than the CW power because the 3 mm intra-cavity fused silica plate used in the CW laser results in slightly smaller laser mode area in the Tm:YLF crystal, resulting in a lower laser threshold.

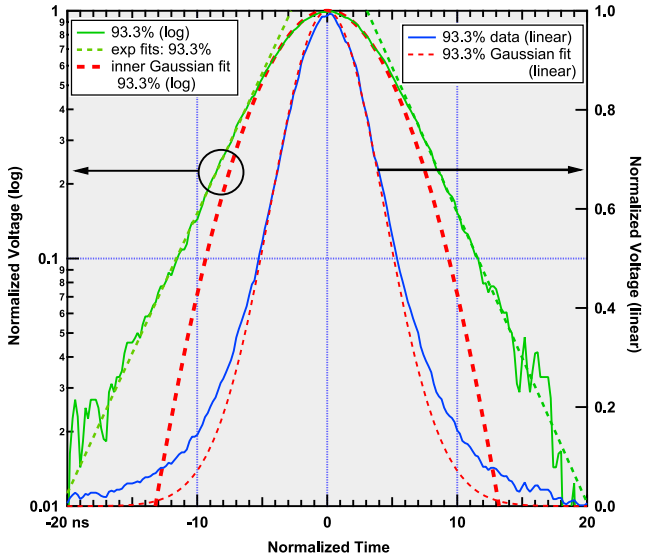

Fig. 7. Q-switched pulse shape for 93.3% saturable absorber.

Q-switched pulse shapes generated by lasers with T_Q = 91.9%, 92.3% and 93.3% are measured using the fast detector described above. FWHM pulse widths are 8.7 ns, 9.3 ns and 10.8 ns for the three versions, respectively. These pulse widths remained unchanged for all pump powers. Fig. 7 shows the Q-switched pulse shape for the laser with the T_Q = 93.3% saturable absorber, plotted on a left logarithmic scale, and a right linear scale.

The linear scale plot shows a significant deviation of the pulse distribution from that of a Gaussian shape, particularly in the tail portions of the pulse. To clarify the nature of this deviation, the log-scale plot of the pulse intensity distribution includes a Gaussian pulse fit, applied to the center portion of the pulse, and an exponential fit, applied to the tail portions of the pulse. A comparison between these fits with the measured pulse clearly shows that while the center portion of the pulse is Gaussian shaped, the tail portions decay exponentially with time.

Q-switched pulse energies are determined either by dividing the measured average power by the pulse repetition frequency, or with a pulse energy sensor (Coherent J-25MT-10 kHz); both methods provide nearly identical values. Pulse energies for the three laser variants, measured as a function of pump power, are shown in Fig. 8.

IV. Finite-Difference Beam Propagation Method (FD-BPM)

The methods we use to model the Tm:YLF PQSL are based on those described in [17] for a Yb:YAG PQSL with smaller and simpler cavity configuration. A finite-difference version of the Helmholtz equation is used to calculate how a single-wavelength laser field propagates with diffraction in the optical cavity of Fig. 1. The wavelength is determined by the 1908 nm gain maximum, also matching the more selective center wavelength of the VBG. The field propagation within the cavity is altered by the effects of non-uniform complex optical permittivities of the inverted Tm:YLF gain medium and loss from the saturable passive Q-switch, Cr^{2+}:ZnS. To reduce

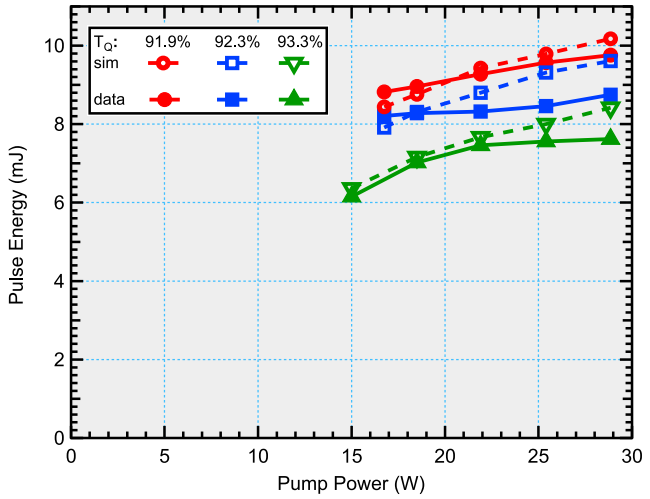

Fig. 8. Measured and simulated Q-switched pulse energies as a function of pump power for lasers for $T_Q = 91.9\%$, 92.3% and 93.3%.

the three-dimensional calculation burden, we assume radial symmetry and use only radial (r) and axial (z) propagation dimensions. Our numerical constraint on the field radial distribution eliminates solutions that vanish at $r = 0$ (corresponding to high-order azimuthal variations, such as the so-called 'donut'-like modes).

Each incremental longitudinal propagation step of the laser field in the cavity uses an efficient numerical solution of a finite-difference tri-diagonal matrix equation, which includes the local complex optical permittivity. The details of this finite-difference method are more fully described in [17]. After the field propagates a full round trip in the laser cavity, the permittivities are updated using the material rate equations and local optical intensities. Our round-trip snapshot approach resembles an earlier simple analytic method [18], which however, assumed transverse uniformity, longitudinal averaging, and instantaneous deterministic Q-switching. Our method requires iterated round-trip propagation, but includes all spatial non-uniformities of the media and laser field, plus phase variations from the optical lens and output coupler. This iteration produces a train of Q-switched pulses, separated by long intervals (typically ~1ms-5ms) of continuously pumped gain recovery. Level sensing of the coherent laser amplitude is used to determine when a pulse starts being generated; the rate-equation time step is then set to one round-trip. Between pulses, the laser field changes more slowly and a coarser time-step is used, typically several thousand round-trip intervals. This allows fewer iterations and shorter computation times.

We begin the calculation with a short period of gain build-up to near-threshold from absorption of a CW pump, described previously. Further details of the subsequent dynamic internal spatial absorption and saturation follow below. The first pulse build-up sees a gain distribution resulting from only the pump (including its self-saturation effects), and decreasing along z. Subsequent pulses evolve from gain that is non-uniformly saturated in r, with dips near $r = 0$. The simulated pulse parameters are evaluated from the last in a train that has approached steady-state inversion saturation and recovery.

The laser cavity is significantly longer (39 mm, compared to 14 mm for Yb:YAG), and is designed for larger mode area, higher pulse energy, and lower repetition rate. For calculation purposes, we assume wide, radial, super-Gaussian apodizations of the VBG and output-coupler reflectance. These help suppress edge build-up of numeric laser field artifacts from the slightly imperfect transparent boundary conditions of the wider mode [17].

As described previously, the laser cavity is designed to maximize the mode size at the passive Q-switch. In the FD-BPM calculations the required intra-cavity divergent lens is modeled as a negative quadratic phase-curvature (thin lens), followed by a uniform length of fused silica (or other desired material) for the lens thickness. The cavity modeling process begins with a Gaussian mode analysis of a passive cavity (neglecting absorption loss) to estimate the initial z = 0 mode size. This is followed by numerical FD-BPM analysis of a CW pumped cavity, in which a passive fused silica plate having the same equivalent diffractive thickness replaces the Q-switch. The CW cavity parameters are the starting point for the PQSL simulations.

Pump absorption near 792 nm is polarized in two distinct bands. We assume the pump emission from the fiber core is unpolarized, so the absorption coefficient is the average of the two 'σ' and 'π'-polarized coefficients at the selected wavelength, generally 792.0 nm. Tm:YLF absorption near 792 nm takes place via pumping into an excited state that rapidly decays into upper lasing manifolds of two nearby Tm^{3+} ions. We neglect residual population of the pump level and its subsequent radiative decay processes. Because of the wavelength constraints and the energy transfer process, the efficiency of an ideal process with two Tm^{3+} excitations for one pump photon is reduced. In our calculation, the reduction is presumed to be the quantum defect between the pump photon energy and two lasing photons; the efficiency is characterized by a pump quantum efficiency factor less than 2:

$$\eta_{qP} = 2\left(1 - \frac{h\nu_P - 2h\nu_L}{h\nu_P}\right) = 1.66$$

This best-case value is lower than 1.88, cited in [19].

Direct spontaneous emission from the initial excited pump level is ignored. Lower Tm concentration than Yb, and larger mode size require longer crystal lengths (e.g. 20.2 mm vs 3 mm) for desired lasing gain. Simple approximations to thermal changes in the cross-sections can be applied, but only in a mode-averaged, static Boltzmann approximation (for practical numerical evaluation). All numerical calculations reported here use 300K temperature. We have calculated the performance degradation from thermal cross-section effects to be small, and of the same order as uncertainty in thermal lensing.

The pump absorption coefficient (α_P) in Tm:YLF is lower than that of Yb:YAG and experiences larger saturation effects, included in our new revised model. The process applies to both the pre-lasing initial inversion build-up interval, and for each FD-BPM time increment, where both lasing and pump both contribute to Tm inversion saturation. A quasi-paraxial approximation is used, assuming longitudinal integration for each radial location. Details are given in the following equations.

The r and z dependent notations of all functions below are suppressed, except for $P(z)$. The spatially continuous rate equations shown here are calculated as discrete finite-difference equations. The equality (=) signs indicate right-to-left assignments in the numeric simulation.

$P \triangleq$ local pump power in Tm^{3+} : YLF;
initial: specified unattenuated distribution

$\rho \triangleq$ local fractional inversion in upper lasing manifold;
initially 0

$\eta_{QP} \equiv$ "2-for-1" pump factor adjusted for quantum defect

$$\Delta\rho = \Delta t \left[\left(\eta_{QP} \sigma_{aP} / h\nu_P \right) P(z) (1 - \rho) - (\rho / \tau_{Tm}) \right]$$

$$\rho = \rho + \Delta\rho$$

$$\alpha_P = N_{Tm} \sigma_{aP} (1 - \rho)$$

$\sigma_{aP} =$ pump absorption coefficient

$$P(z) = \exp\left(- \int_0^z \alpha_P dz \right) P_{in}(z)$$

In each time step Δt, the inversion is modified by pump absorption and radiative decay. The new inversion resets the local absorption coefficient, and this alters the subsequent power-dependent internal pump distribution. After an initial sub-threshold interval, the same type of step procedure is used during lasing simulation, with laser saturation factors added to the first inversion rate-equation increment. In all cases, the dynamically adjusted $P(z)$ is then used for calculating the next time step evolution. An internal integral calculation with optimized matrix operations applied to the exponential absorption speeds up the z-dependent pump saturation calculation, including the implicit r-dependence. The time increment is adjusted automatically to be one laser cavity round-trip interval when the lasing field exceeds a very low threshold. Between Q-switched pulses, when the lasing field magnitude is low, $\Delta t$is much coarser. During the lasing iterations, additional saturating terms from the lasing intensity are added to the inversion rate equations within the two active media.

Even though the effects of thermal lensing are expected to be small, they are significant in our cavity designs, where beam divergence is maximized within limits of lasing stability. In the previous Yb: YAG thermal model radial symmetry was a good approximation, so the thermal refractive index effects were incorporated in the real part of the complex dielectric permittivity. In addition, the r and z-dependent temperature distribution was numerically evaluated as the solution of a radial diffusion equation, again using an efficient tri-diagonal finite-difference matrix equation. In Tm:YLF the asymmetric heat-sinking and anisotropy of the YLF thermal conductivity call into doubt the accuracy or benefits of a radial-symmetry diffusive numerical analysis of the temperature. Instead, we apply a single, thin, effective thermal lens placed at the pumped face of the Tm:YLF crystal. This is where the absorbed pump power is maximum, and its radial distribution is known. An estimate of the thermal lens focal length may be found from formulas in the literature [20], [21], [22] but a semi-empirical approach is simpler. We assume a (1/pump-power) dependence and proportionality to pump beam area (at half-maximum) for the divergent focal length; an effective adjusted thermal focal length coefficient provides the best fit with measured output power data (see the CW analysis below). Flat-phase apodization on the outer quadratic phase curvature of both the thermal lens and the divergent fused silica lens help suppress high-spatial frequency phase cycles near the calculation boundary.

Measured CW characteristics have usually accompanied PQSL evaluation, so a CW analysis version was developed, with the Q-switch plate replaced by an AR-coated fused silica plate. Equivalent ray-trace (ABCD matrix) diffractive distances are used for the two air-plate-air cases. The small change in temporal cavity length (round-trip time) is not relevant in CW FD-BPM modeling. It does play a role in interpreting the CW temporal fluctuations, so the normal effective optical propagation length of the cavity is calculated. The different PQSL effective propagation length sets the laser round-trip time (the minimum simulation time increment).

Only a single very coarse calculation time-step is used for CW modeling. A long pre-lasing interval is applied, and then a relatively large initial laser complex field is launched. This avoids a long interval of build-up from ASE, so the initial part of the iterated solution does not reflect true time-domain behavior. Damped relaxation oscillations are observed in the convergence process, but these are not quantitatively identical to actual physical relaxations. However, they are caused by the same coupling interactions between stimulated emission and inversion. The CW analysis executes many time faster than that of the PQSL because of the coarser time step and omission of all Q-switch rate-equation calculations. To a good approximation, the thermal lensing parameters that give the most accurate CW results can be applied in the PQSL model. In general, with high-repetition-rate pulsing, the simulated PQSL and CW average powers are comparable, with the PQSL output power slightly lower.

The passive Q-switch material (Cr^{2+}-doped ZnS) is chosen because the vibronic Cr^{2+} transition absorbs at the laser wavelength, 1908 nm, and is readily saturated. Similar materials also have had a wide range of applications of NIR lasers in their own right, with published parameters useful for our PQS application [23], [24], [25]. The earlier PQS for the Yb:YAG laser was Cr:YAG; when fully saturated, the Cr^{2+} ground manifold became completely inverted. In the zincblende hosts, the degree of Cr^{2+}inversion depends on the absorption and emission cross-sections. The broad nature of the PQS transition gives rate equations for Cr^{2+} and Tm^{3+} with the same form, but greatly different optical parameters. Full PQS saturation occurs at laser-wavelength optical transparency, where upward and downward stimulated transition rates are equal. The Cr^{2+} density for an individual Q-switch is calculated from its thickness, measured (nominal) unsaturated transmission, and measured saturated transmission (typically ~98%).

Table II contains simulated laser characteristics of pulsed operation. The pulse average power and energy are also shown for other pump powers in the preceding figures.

TABLE I
SYMBOL DESCRIPTIONS AND VALUES

Symbol	Description	Units	Value
σ_{aP}	Pump Tm absorption cross-section	cm^2	7.93×10^{-21}
σ_{eP}	Pump Tm emission cross-section	cm^2	1.74×10^{-21}
σ_{aL}	Laser Tm absorption cross-section	cm^2	1.28×10^{-21}
σ_{eL}	Laser Tm emission cross-section	cm^2	2.42×10^{-20}
τ_{Tm}	Tm spontaneous emission lifetime	s	14.0×10^{-3}
N_{Tm}	Tm ion density (laser); 3.5% doping	cm^{-3}	1.39×10^{21}
σ_{aQ}	Cr^{2+}:ZnS absorption cross-section	cm^2	2.95×10^{-19}
σ_{eQ}	Cr^{2+}:ZnS emission cross-section	cm^2	6.64×10^{-19}
τ_Q	Cr^{2+}:ZnS spontaneous emission lifetime	s	5.0×10^{-6}

TABLE II
PULSE SIMULATED CHARACTERISTICS AT 28.9 W PUMP

Cr^{2+}:ZnS transm. (%)	Pulse Energy (mJ)	Pulse duration, FWHM (ns)	Average power (W)	Mode FW($1/e^2$) at OC (mm)	Mode FW($1/e^2$) Tm:YLF (mm)
91.9	10.2	7.8	6.9	1.43	0.624
92.3	9.6	8.2	6.9	1.42	0.624
93.3	8.4	9.5	7.2	1.39	0.611

V. DISCUSSION AND SUMMARY OF RESULTS

The model relies on input parameters from published data or other independent variables such as cavity component properties and placement, so there are essentially no adjustable parameters. The exception is the approximation for the small, discrete-valued negative thermal lensing. In comparing CW and average output power vs pump power, the simulated slope efficiencies generally show very good agreement with the data. However, there is a consistent trend for the average power simulations to have slightly lower pump thresholds. However, the model does have inherent limitations, such as the assumptions of radial symmetry and coherent single-frequency laser operation.

We assume lasing in a fundamental transverse mode (without specifying its shape), because data is gathered only where no higher-order transverse-modes are observed. CW simulations show output intensity profiles different from Gaussians. The simulated profiles are generally flat near $r = 0$, with noticeable radial fluctuation that increases with pump power. The model's assumptions allow for such non-monotonic amplitude variation. In a laser cavity allowing many resonant modes, contributions from high-order radial modes (but with $l = 0$) would oscillate at different frequencies. Our model cannot include this, unless such modes are generated and propagated independently so that their intensities add incoherently. Of the two situations, improper coherent addition at one frequency would result in higher power than is observed, and might explain our simulated output power results exceeding the measured data. However, there is no experimental evidence of the lowest order $l = 1$ ('donut') mode occurring, which often is often the easiest to excite, before high-order $l = 0$ modes. This matter is currently unresolved.

Measurements such as shown in Fig. 5 clearly show that multiple axial modes are present, more so in CW operation. We suspect that the observed multiple frequencies (e.g. from longitudinal hole burning) have higher losses away from the VBG center frequency, causing lower efficiency. We have presented clear experimental evidence for mode-beating at the cavity round-trip frequency (Fig. 6b), so such CW axial modes are present. Q-switched operation also shows multiple output wavelengths, so the same issue can exist in that regime also.

The agreement of measured and simulated pulse energies is good (see Fig. 8), including three different Q-switch cases. Both experimental and simulated pulse energies increase monotonically with the pump powers; this increase is correlated with larger simulated mode areas in the YLF at higher pump powers. The middle value ($T_Q = 92.3\%$) shows the largest discrepancies between data and simulation; this disparity can be attributed to experimental factors such as small, thermally induced, changes in cavity alignment with pump power. In all cases, the dependence of pulse energy on pump power is relatively weak. The experimentally observed trend for increasing pulse energy and shorter pulse width for lower PQS transmission (higher lasing hold-off) is also predicted by simpler models [18]. Such simple models do not predict energy variation with pump power.

The temporal pulse shapes in both our simulations and measured data show linear exponential tails on leading and trailing edges, as opposed to commonly assumed symmetric Gaussian quadratic tails. The leading edge tail is characteristic of exponential, unsaturated gain build-up of ASE; the trailing-edge tail shows photon decay from the lossy cavity. The short intermediate quasi-Gaussian pulse contains even more complicated features of PQS saturation, followed by laser saturation and depletion of the gain to sub-threshold levels.

The tower work-station computer used in this work had a standard Intel(R) Core(TM) i5-7500 CPU operating at 3.4 GHz. Depending on the pump and cavity details, the simulations had a wide-range of execution times, ranging from a few minutes to over an hour. A significant fraction of the time was spent in the high-level, interactive software [26] displaying regularly monitored graphical output. The longest times were those of PQSL simulations at low pump powers, which gave the lowest pulse rates and required longer times to ensure that steady-state pulsing was obtained. The long $\sim$14 ms Tm^{3+} radiative decay rate also added to the longer simulation times.

The versatility of the model, combined with its nearly *ab initio* nature, offers a trade-off between overall accuracy *vs* faster multi-parameter comparisons using other models, but with approximated input coefficients or functions.

REFERENCES

[1] L. A. Hardya and N. M. Frieda, "Comparison of first-generation (1908 nm) and second-generation (1940 nm) thulium fiber lasers for ablation of kidney stones," *Opt. Eng.*, vol. 58, no. 9, 2019, Art. no. 096101.

[2] B. Cole et al., "Compact and efficient mid-IR OPO source pumped by a passively Q-switched Tm:YAP laser," *Opt. Lett.*, vol. 43, no. 5, pp. 1099–1102, 2018.

[3] B. Cole, L. Goldberg, and S. Chinn, "Near-IR, blue, and UV generation by frequency conversion of a Tm:YAP laser," in *Proc. SPIE*, vol. 10511, pp. 141–147, Feb. 2018.

[4] R. C. Stoneman and L. Esterowitz, "Efficient 1.94-μm Tm:YALO laser," *IEEE J. Sel. Topics Quantum Electron.*, vol. 1, no. 1, pp. 78–81, Apr. 1995.

[5] J. Vetrovec, D. A. Copeland, and A. S. Litt, "Wide-bandwidth ceramic Tm:Lu_2O_3 amplifier," in *Proc. SPIE*, vol. 9834, pp. 18–27, May 2016.

[6] Y. Shen, X. Duan, J. Yuan, T. Dai, B. Yao, and Y. Wang, "Investigation of high-power diode-end-pumped Tm:YLF laser in slab geometry," *Appl. Opt.*, vol. 54, no. 8, pp. 1958–1962, 2015.

[7] A. Meissner, J. Li, I. Lopez-Perez, S. Yang, M. Hoefer, and D. Hoffmann, "200-W Tm:YLF INNOSLAB laser," in *Proc. SPIE*, vol. 8599, pp. 250–256, May 2013.

[8] L. Gorajek et al., "High repetition rate, tunable, Q-switched diode pumped Tm:YLF laser," *Opto-Electron. Rev.*, vol. 17, no. 4, pp. 309–317, Jan. 2009.

[9] B. Cole, L. Goldberg, and A. D. Hays, "High-efficiency 2 μm Tm:YAP laser with a compact mechanical Q-switch," *Opt. Lett.*, vol. 43, pp. 170–173, Jan. 2018.

[10] R. Faoro et al., "Passively Q-switched Tm:YLF laser," *Opt. Lett.*, vol. 37, no. 9, pp. 1517–1519, 2012.

[11] Y. Dai, Y. Li, X. Zou, B. Jiang, Y. Hang, and Y. Leng, "Compact passively Q-switched Tm:YLF laser with a polycrystalline Cr^{2+}:ZnS saturable absorber," *Opt. Laser Technol.*, vol. 57, pp. 202–205, Apr. 2014.

[12] V. Canbaz, L. Yorulmaz, and A. Sennaroglu, "2.3-μm Tm^{3+}:YLF laser passively Q-switched with a Cr^{2+}:ZnSe saturable absorber," *Opt. Lett.*, vol. 42, no. 9, pp. 1656–1659, 2017.

[13] B. Cole and L. Goldberg, "Highly efficient passively Q-switched Tm:YAP laser using a Cr^{2+}:ZnS saturable absorber," *Opt. Lett.*, vol. 42, no. 12, pp. 2259–2262, 2017.

[14] A. Korenfeld, D. Sebbag, U. Ben-Ami, E. Shalom, G. Marcus, and S. Noach, "High pulse energy passive Q-switching of a diode pumped Tm:YLF laser by Cr^{2+}:ZnSe," *Laser Phys. Lett.*, vol. 12, no. 4, 2015, Art. no. 045804.

[15] E. R. Hale, I. Divliansky, and L. Glebov, "Passively Q switched dual channel Tm:YLF laser by intracavity spectral beam combination with, volume Bragg grating," *Opt. Exp.*, vol. 26, no. 13, pp. 16670–16678, 2018.

[16] L. Goldberg, V. King, B. Cole, and A. Hays, "Passively Q-switched Tm:YLF laser generating 15 mJ, 600 kW peak power pulses," in *Proc. SPIE*, vol. 11664, pp. 23–29, Mar. 2021.

[17] S. R. Chinn, J. H. Leach, C. McIntosh, A. D. Hays, and L. Goldberg, "Numeric multi-dimensional (r, z, t) analysis method for compact Yb^{3+}:YAG end-pumped, passively Q-switched lasers," *IEEE J. Quantum Electron.*, vol. 57, no. 1, pp. 1–15, Feb. 2021.

[18] C. D. Nabors, "Q-switched operation of quasi-three-level lasers," *IEEE J. Quantum Electron.*, vol. 30, no. 12, pp. 2896–2901, Dec. 1994.

[19] G. Li, H. Liu, F. Lu, X. Wen, Y. Gu, and Y. Wang, "Analysis on preferential free running laser wavelength and performance modeling of Tm^{3+}-doped YAP and YLF," *Appl. Opt.*, vol. 53, pp. 4987–4996, Aug. 2014.

[20] S. Chenais, F. Balembois, F. Druon, G. Lucas-Leclin, and P. Georges, "Thermal lensing in diode-pumped ytterbium lasers—Part I: Theoretical analysis and wavefront measurements," *IEEE J. Quantum Electron.*, vol. 40, no. 9, pp. 1217–1234, Sep. 2004.

[21] S. Chenais, F. Balembois, F. Druon, G. Lucas-Leclin, and P. Georges, "Thermal lensing in diode-pumped ytterbium lasers—Part II: Evaluation of quantum efficiencies and thermo-optic coefficients," *IEEE J. Quantum Electron.*, vol. 40, no. 9, pp. 1235–1243, Sep. 2004.

[22] S. Chenais, F. Druon, S. Forget, F. Balembois, and P. Georges, "On thermal effects in solid state lasers: The case of ytterbium-doped materials," *Prog. Quantum Electron.*, vol. 30, no. 4, pp. 89–126, 2006.

[23] S. B. Mirov, V. V. Fedorov, D. Martyshkin, M. Mirov, and S. Vasilyev, "Progress in mid-IR lasers based on Cr and Fe-doped II–VI chalcogenides," *IEEE J. Quantum Electron.*, vol. 21, no. 1, pp. 1–19, Jan./Feb. 2015.

[24] S. B. Mirov et al., "Frontiers of mid-IR lasers based on transition metal doped chalcogenides," *IEEE J. Sel. Topics Quantum Electron.*, vol. 24, no. 5, pp. 1–29, Sep. 2018.

[25] A. G. Bluiett, U. Hömmerich, R. T. Shah, S. B. Trivedi, S. W. Kutcher, and C. C. Wang, "Observation of lasing from Cr^{2+}:CdTe and compositional effects in Cr^{2+}-doped II–VI semiconductors," *J. Electron. Mater.*, vol. 31, no. 7, pp. 806–810, Jul. 2002.

[26] *IGOR Pro*, WaveMetrics, Lake Oswego, OR, USA, 2023. [Online]. Available: https://wavemetrics.com/products/igorpro

Stephen R. Chinn (Life Senior Member, IEEE) was born in Baltimore, MD, USA. He received the B.S., M.S., and Ph.D. degrees in electrical engineering from the Massachusetts Institute of Technology (MIT), Cambridge, MA.

He was with AT&T Bell Laboratories, MIT Lincoln Laboratory, and the General Electric Electronics Laboratory. Since 2002, he has been with the U.S. Army DEVCOM C5ISR Night Vision and Electronic Sensors (now RTI) Directorate, as a Civilian Employee and a Contractor, where he performs research and development on advanced laser and electro-optic sensor systems.

Lew Goldberg was born in Chervyen, Belarus. He received the B.S. degree in electrical engineering from Tufts University in 1973, the M.S. degree in electrical engineering from Carnegie Mellon University in 1974, and the Ph.D. degree in applied physics from the University of California at San Diego in 1979.

He was an Assistant Professor with UCSD in 1980, Naval Research Laboratory from 1980 to 2000, Keopsys Inc. from 2000 to 2005, and U.S. Army DEVCOM C5ISR Night Vision and Electronic Sensors (now RTI) Directorate since 2005, where he was the Head of the Laser Branch, he performed research and development on advanced lasers, electro-optic devices, and optical systems.

Vernon King was born in Blytheville, AR, USA. He received the B.S. degree in physics from the University of Arkansas, Fayetteville, in 1982.

He joined the Laser Division, U.S. Army Night Vision and Electronic Sensors (now RTI) Directorate, in 1984, and participated in its laser diode fabrication program, developing procedures for applying optical coatings to laser diode facets and implementing instrumentation to accurately measure laser diode characteristics. He set up instrumentation for measuring the impact of laser diodes on several U.S. Army programs. He received a 2003 Army RDA Award for work on the patented (Er,Yb) glass micro-laser. He continues to work on diode-pumped solid-state lasers.

Jeffrey H. Leach received the M.S. degree in electrical engineering from the Virginia Polytechnic Institute and State University in Blacksburg, VA, USA, and the Ph.D. degree in electrical engineering from The Catholic University of America, Washington, DC.

He focused on electro-optics of LIDAR systems. He has been with the U.S. Army DEVCOM C5ISR Night Vision and Electronics Sensors (now RTI) Directorate as an Electronics Engineer since 2003. He currently works on robust electro-optic systems.

Alan D. Hays received the M.S. degree in physics from the University of South Florida, Tampa, in 1987, and the Ph.D. degree in electrical engineering from The Catholic University of America, Washington, DC, in 2015. He studied opto-thermal stresses, and methods for improving laser brightness.

In 2001, he joined the U.S. Army DEVCOM C5ISR Night Vision and Electronics Sensors (now RTI) Directorate as a Research Scientist. He currently works on compact solid-state lasers and electro-optic systems.

Brian Cole received the Ph.D. degree in ceramic science and engineering from Rutgers University, New Brunswick, NJ, in 1996.

At Rutgers University, he fabricated and developed novel fiber optics via MCVD for active applications. In 1996, he joined the Infrared Materials Group, Naval Research Laboratory, Washington, DC, where he was responsible for development of high purity rare-earth doped chalcogenide-based optical materials and fiber optics for applications in the mid-IR. Since 2000, he has been with Keopsys Inc., Hawai'i Natural Energy Institute, University of Hawai'i, Mānoa, and the U.S. Army DEVCOM C5ISR Night Vision and Electronic Sensors (now RTI) Directorate. He is currently interested in compact diode pumped solid-state lasers and frequency conversion processes from the deep-UV to LWIR.